Parametric study on thermal and hydraulic characteristics of laminar flow in microchannel heat sink with fan-shaped ribs on sidewalls – Part 2: pressure drop

Lei Chai[a, *], Guo Dong Xia[b], Hua Sheng Wang[a]

[a] School of Engineering and Materials Science, Queen Mary University of London, Mile End Road, London E1 4NS, UK

[b] Key Laboratory of Enhanced Heat Transfer and Energy Conservation, Ministry of Education, College of Environmental and Energy Engineering, Beijing University of Technology, Beijing, China

Abstract This second part of a three-part study concerns pressure drop of laminar flow in microchannel heat sinks with water and silicon used as fluid and solid for the computational domain. In the rectangular microchannel with width of 0.1 mm and depth of 0.2 mm, the repeating aligned or offset fan-shaped ribs are mounted to the channel sidewalls. To examine the influence of fan-shaped rib's geometry on thermal and hydraulic characteristics of laminar flow, three non-dimensional variables, representing the width (0.005-0.4 mm), height (0.005-0.025 mm) and spacing (0.2-5 mm) of fan-shaped ribs are designed. The present study firstly presents the pressure distributions in microchannels to analyze the local hydraulic characteristics, and then examines the local pressure and friction factor along the flow direction for different geometry of fan-shaped ribs. Results show that the fan-shaped ribs can lead to large increase of local pressure in comparison with the smooth microchannel, especially for the aligned fan-shaped ribs. Further, the effect of fan-shaped ribs' geometry on

* Corresponding author. Tel.: +44 20 7882 7306.

E-mail address: l.chai@qmul.ac.uk (Lei Chai).

the average friction factor has been investigated. Results show that with the increase of fan-shaped ribs' width, the friction factor ratio of the studied microchannels to the smooth one firstly decreases and then increases. The increase of fan-shaped ribs' height and decrease of ribs' spacing can lead to the extreme increase of average friction factor, especially for the microchannels with aligned fan-shaped ribs. For Reynolds number ranging from 187 to 715, the microchannels with aligned fan-shaped ribs show the average friction factor 1.1-8.28 times larger than the smooth one, while those with offset fan-shaped ribs show 1.22-6.27 times higher. New pressure drop correlations for such microchannel heat sinks are developed, which fit the present data with a mean absolute error of 13.2% for the ones with aligned fan-shaped ribs and 13.5% for the ones with aligned fan-shaped ribs.

Key words microchannel heat sink; fan-shaped ribs; pressure drop; friction factor

1. Introduction

Liquid cooled microchannel heat sinks have been used in a variety of devices, such as the cooling of electronic devices, automotive heat exchangers, laser process equipment and aerospace technology, etc. However, the application of microchannel heat sinks in electronics cooling imposes severe constraints on the system design. For a given heat dissipation rate, the flow rate, pressure drop, fluid temperature rise, and fluid inlet to surface temperature difference requirements necessitate optimization of the channel geometry [1]. And largely due to rapid increase in power density and miniaturization of electronic packages, very high heat flux chip cooling requires smaller hydraulic diameter and larger flow rate, which can lead to

very high pressure drop. Further, in order to solve the problem of the tremendously increased chip-level heat fluxes, several more efficient cooling methods have been developed to keep the device at its allowable temperature, but the heat transfer augmentation is always concerned with penalty in terms of increased friction factor resulting in higher pressure drop. Therefore, the fundamental understanding of flow characteristics is essential in design and process control of microfluidic devices [2, 3].

Xu et al. [4, 5] experimentally and numerically studied laminar flow and heat transfer in a microchannel heat sink comprising parallel longitudinal microchannels with several transverse microchambers. They found that the overall heat transfer was greatly enhanced and the pressure drop was similar or decreased than the conventional one for Reynolds number in the range of 169-994. Subsequently, Chai et al. [6] introduced the staggered rectangular ribs into the transverse microchambers and studied the laminar flow characteristics in such heat sinks. They found that the interrupted microchannel with ribs was suitable for the operating condition as Reynolds numbers lower than 600, and if Reynolds numbers was larger than 600, the interrupted microchannel without ribs performed better, due to the tremendously increased pressure drop in such heat sinks.

Promvonge et al. [7] numerically investigated laminar flow and heat transfer in a three-dimensional isothermal wall square channel with 45º-angled baffles. They found that the heat transfer augmentation of 150-850% was associated with enlarged pressure loss ranging from 2 to 70 times above the smooth channel for Reynolds number in the range of 100-1000. Liu et al. [8] experimentally investigated the fluid flow and heat transfer in microchannel heat sink with longitudinal vortex generators (LVGs). For LVGs with different

number of pairs and angles of attack, the improved heat transfer performance by 9-90% was associated with the increased pressure drop by 34-169% for Reynolds numbers in the range of 170-1200. Subsequently, Ebrahimi et al. [9] numerically investigated the liquid flow and conjugated heat transfer performance in such microchannel heat sinks. The results showed that for Reynolds number ranging from 100 to 1100, there was a 2-25% increase in the Nusselt number for microchannels with LVGs, while the friction factor increased by 4-30%.

Chai et al. [10, 11] experimentally and numerically studied the laminar flow and heat transfer characteristics in microchannel heat sinks with periodic expansion-constriction cross-sections. They found that such microchannel heat sinks had prominent advantages over the smooth one. For Reynolds number ranging from 147 to 752, the heat transfer coefficient increased by 12.5-72.3% while the friction factor increased by -10-24% for the microchannel heat sink with fan-shape reentrant cavities; the heat transfer coefficient increased by 21.5-80.4% while the friction factor increased by -10-27% for the one with triangular reentrant cavities. Xia et al. [12, 13] numerically investigated the effect of geometric parameters on water flow and heat transfer characteristics in such microchannel heat sinks. They found that the geometric parameters had a significant influence on heat transfer and pressure drop. The reentrant cavities could lead to better heat transfer performance, and result in increased or decreased pressure drop dependent on the Reynolds number and geometric parameters.

Ghaedamini et al. [14] numerically studied the developing forced convection in converging-diverging microchannel heat sink and systematically investigated the effects of channel aspect ratio and amplitude of the converging-diverging profiles for Reynolds

numbers ranging from 50 to 200. They found that due to the fluid mixing arising from a pair of recirculating vortices in the converging-diverging channels, the heat transfer performance was always significantly improved with the potential of much smaller pressure drop penalty than the heat transfer enhancement. Sui et al. [15, 16] and Mohammed et al. [17] experimentally and numerically studied laminar flow and heat transfer in wavy microchannel heat sinks. They all concluded that the heat transfer performance of the wavy microchannels was much better than the straight one, while the pressure drop penalty could be much smaller than the heat transfer enhancement.

Based on the passive heat transfer enhancement methods, Chai et al. [18] introduced the offset ribs to the two opposite channel sidewalls for microchannel heat sink. For Reynolds number ranging from 190 to 838, the heat transfer coefficient increases 42-95% while the friction factor 1.93-4.57 times higher than the smooth one, dependent on the geometry of offset ribs. In order to obtain the insight into the fluid flow and heat transfer mechanisms and present a systematic and detailed analysis for such microchannel heat sinks, the present paper focuses on the geometric parameters of both aligned and offset fan-shaped ribs on thermal and hydraulic characteristics. In the first part of a three-part study, the effects of such parameters on heat transfer characteristics have been systemically investigated. As the second part of the three-part study, the present paper concerns pressure drop for laminar flow in such microchannel heat sinks. As the passive microstructure makes the laminar flow characteristics to be quite different from those in the smooth channel, it is therefore necessary to undertake fundamental investigations to understand the difference in these characteristics.

2. Numerical solution and procedure

2.1. Governing equations

The material of heat sink base is silicon and the coolant is deionized water. The flow and heat transfer in microchannel is assumed to be three-dimensional, incompressible and steady state laminar flow. Some of the properties are allowed to vary with temperature. The continuity, momentum and energy equations for the problem can be written as

$$\nabla \cdot (\rho_{\mathrm{f}} \vec{u}) = 0 \tag{1}$$

$$\nabla \cdot \left(\rho_{\mathrm{f}} \vec{u}\vec{u} \right) = -\nabla p + \nabla \cdot \left[\mu_{\mathrm{f}} (\nabla \vec{u} + \nabla \vec{u}^{\mathrm{T}}) \right] \tag{2}$$

$$\nabla \cdot \left(\rho_{\mathrm{f}} c_{\mathrm{pf}} \vec{u} T \right) = \nabla \cdot \left(k_{\mathrm{f}} \nabla T \right) + \mu_{\mathrm{f}} (\nabla \vec{u} + \nabla \vec{u}^{\mathrm{T}}) \cdot \nabla \vec{u} \tag{3}$$

where $\vec{u}$ is the fluid velocity vector, p is the hydrodynamic pressure, ρ_{f}, μ_{f}, c_{pf} and k_{f} are the water density, dynamic viscosity, specific heat capacity and thermal conductivity, respectively, whose dependence on temperatures are given by Incropera [19].

In addition, a conjugate heat transfer has to be solved by considering the heat conduction in the heat sink base to obtain the thermal boundary condition on the channel inner wall/ fluid contact surface. The heat conduction equation in the heat sink base is expressed as

$$\nabla \cdot \left(k_{\mathrm{s}} \nabla T \right) = 0 \tag{4}$$

where k_{s} is the thermal conductivity of silicon and is set as a constant of 148 $\mathrm{W \cdot m^{-1}\ K^{-1}}$ in the computations.

2.2. Computational domain and boundary conditions

To save the computation time and take advantage of symmetry boundary condition, a control volume containing a single microchannel and surrounding solid along with the base is selected for developing the fluid flow and heat transfer model. As shown in Fig. 1a, the length,

width and height of the computational domain are 10 mm, 0.25 mm and 0.35 mm, respectively. The depth of microchannel is 0.2 mm and the width of the microchannel without ribs (W_c) is 0.1 mm. The serial aligned or offset fan-shaped ribs are introduced into the two parallel sidewalls, respectively. The geometric parameters of fan-shaped ribs examined in this paper are shown in Fig. 1b, including the width (W_r), the height (H_r), and the spacing (S_r). Based on these geometric parameters, three non-dimensional variables are designed to analyze their effects on thermal and hydraulic characteristics. They are the ratio of the width of rib to the spacing (W_r/S_r), the ratio of the height of rib to the width of the two parallel sidewalls (H_r/W_c), and the ratio of the spacing of ribs to the width of the two parallel sidewalls (S_r/W_c), respectively. Meanwhile, a smooth microchannel heat sink without fan-shaped ribs is selected for comparison.

Boundary conditions for this simplified computational domain are specified as follows. At the microchannel inlet (x = 0), the water velocity (u_{in}) and the water temperature (T_{in} = 293 K) are specified. The u_{in} is assumed uniform in x direction and to be zero in y and z direction. The u_{in} are chosen as the water average velocity $\bar{u}$ = 1, 2, 3, 4 and 5 $m \cdot s^{-1}$ in the constant cross-section region. The remainder of the computational domain entrance is occupied by the silicon, where the velocities are zero and the surface is adiabatic. At the exit of the computational domain (x = 10 mm), a pressure-outlet boundary condition (p_{out} = 0 for gauge pressure) is applied for the microchannel outlet, and zero velocities and adiabatic surface for the silicon. Symmetry is imposed on the left (y = 0.25 mm) and right (y = 0) boundaries. At the bottom boundary (z = 0), the velocities are zero and a constant heat flux ($q_w = 10^6$ $W \cdot m^{-2}$) is imposed at the bottom wall. The top wall (z = 0.35 mm) is assumed to be adiabatic and has

zero velocities.

2.3. Solution methods and convergence criteria

The computational fluid dynamics solver ANSYS FLUENT 12.0, which uses a finite volume method, was used for numerical simulations in the present work. The discretized governing equations were solved using the SIMPLEC algorithm option. In the present study, a solution is deemed converged when the normalized residual values are less than 10^{-5} for all variables. The numerical code is verified in a number of ways to ensure the validity. The grid independence test is similar to Chai et al. [15]. In order to further check the accuracy and reliability of this physical model, numerical results of laminar flow in the smooth microchannel have been performed by comparing with the experimental results from Chai et al. [11] as shown in Fig. 2. It is shown that the comparison for friction factor is in good agreement.

2.4. Data acquisition

Parameters characterizing the laminar flow in the microchannel are presented as follows. The Reynolds number is defined as

$$Re = \frac{\rho_f \bar{u} D_h}{\mu_f} \tag{5}$$

where ρ_f is the volume average fluid density, $\bar{u}$ is the average flow velocity mentioned above, D_h is the hydraulic diameter calculated based on the constant cross-section region, μ_f is the mass average fluid dynamic viscosity. The ρ_f and μ_f are defined as

$$\rho_{\mathrm{f}}=\frac{\int \rho_{\mathrm{f,i}} dV}{V} \tag{6}$$

$$\mu_{\mathrm{f}}=\frac{\int \mu_{\mathrm{f,i}} \rho_{\mathrm{f,i}} dV}{\int \rho_{\mathrm{f,i}} dV} \tag{7}$$

The local Fanning friction factor is calculated by

$$f_{\mathrm{x}}=\frac{(p_{\mathrm{in}}-p_{\mathrm{x}})D_{\mathrm{h}}}{2\rho_{\mathrm{f}}(x-x_{\mathrm{in}})u_{\mathrm{m}}{}^{2}} \tag{8}$$

The average Fanning friction factor is expressed by

$$\overline{f}=\frac{(p_{\mathrm{in}}-p_{\mathrm{out}})D_{\mathrm{h}}}{2\rho_{\mathrm{f}}L\overline{u}^{2}} \tag{9}$$

where L is the whole length of the microchannel, p_{in} is the mass-weighted average pressure in the channel inlet and p_{out} is the pressure in the channel outlet. The p_{x} is defined as

$$p_{\mathrm{x}}=\frac{\int p_{\mathrm{x,i}} \rho_{\mathrm{f,i}} \left|\mathbf{u}\cdot d\mathbf{A}\right|}{\int \rho_{\mathrm{f,i}} \left|\mathbf{u}\cdot d\mathbf{A}\right|} \tag{10}$$

The p_{in} is defined as

$$p_{\mathrm{in}}=\frac{\int p_{\mathrm{in,i}} \rho_{\mathrm{f,i}} \left|\mathbf{u}\cdot d\mathbf{A}\right|}{\int \rho_{\mathrm{f,i}} \left|\mathbf{u}\cdot d\mathbf{A}\right|} \tag{11}$$

3. Results and discussion

3.1. Parametric study on local hydraulic characteristics

Figure 3 presents the pressure distribution and Fig. 4 shows the p_{x} along the flow direction with x in the range of 6.0 to 6.8 mm in the plane of z = 0.25 mm as Re = 443. The corresponding velocity contour and streamlines have been shown in the first part of the three-part study. For the smooth microchannel heat sink (MCHS), the pressure continuously decreases due to frictional losses along the microchannel; For the microchannel with fan-shaped ribs, the pressure drop consists of not only the term along the microchannel, but

also the term resulting from the fan-shaped ribs. For the microchannel heat sink with aligned fan-shaped ribs (MCHS-AFR), the effect of fan-shaped ribs on pressure drop is mainly caused by the changed flow passage. As water flows across the offset ribs, the pressure rapidly decreases with the constriction of flow passage and slowly increases with the expansion of flow passage. Further, the pressure in the constant cross-section region still increases very slowly, leading to the inverse pressure gradient in the channel, which is beneficial to develop the recirculation in the downstream of fan-shaped ribs. From Fig. 4, it is noted that the constriction of flow passage results in large pressure drop. For the microchannel heat sink with offset fan-shaped ribs (MCHS-OFR), the effect of fan-shaped ribs on pressure drop is mainly caused by changed flow direction and the changed flow passage. Generally, the pressure drops tortuously without obvious inverse pressure gradient.

Figures 5a and 5b respectively show the effects of W_r on p_x and f_xRe along the flow direction as Re = 443, where the non-dimensionalized length is defined as ($x^+ = x/(D_hRe)$). The geometry of fan-shaped ribs used in these figures is W_c = 0.1 mm, H_r = 0.025 mm, S_r = 0.4 mm and W_r = 0.1, 0.2, 0.3 and 0.4 mm. From Fig. 5a, it is noticed that the fan-shaped ribs lead to extreme increase in local pressure in comparison with MCHS, and the aligned fan-shaped ribs result in more increase than the offset ones. The pressure difference at a given x position is very small between the cases with W_r/S_r = 0.25 and 0.5, while increases with the increase of W_r as $W_r/S_r > 0.5$ for both MCHS-AFR and MCHS-OFR. The aligned fan-shaped ribs result in obvious pressure fluctuation with the changed flow passage, and the vibration amplitude becomes a little smaller with the increase W_r/S_r. For the MCHS-OFR, the pressure generally drops along the flow direction without obvious pressure fluctuation. Along the

whole length of microchannel, the pressure drop ($\Delta p = p_{in} - p_{out}$) is 44.78 kPa for MCHS, but 179.76, 187.62, 216.86 and 244.63 kPa respectively for MCHS-AFR with W_r/S_r = 0.25, 0.5, 0.75 and 1, and 109.97, 120.78, 160.63 and 202.67 kPa respectively for MCHS-OFR with W_r/S_r = 0.25, 0.5, 0.75 and 1. From Fig. 5b, it can be found that the fan-shaped ribs lead to obviously different local friction factor. At the channel inlet, the friction factor is very large, but rapidly decreases along the flow direction, corresponding to the hydrodynamic developing region. For the MCHS, the dimensionless length of the hydrodynamic developing region x^+ is 0.055 as indicated by Phillips [20], and in the range of $x^+ > 0.055$ the f_xRe decreases very slowly with increase of x^+, due to the decrease of viscosity caused by the increase of fluid temperature, as indicated Chai et al. [11]. For the microchannel with fan-shaped ribs, the following phenomena could be identified. At the channel inlet, the f_xRe values are larger than that of the MCHS, which is caused by the larger pressure gradient resulting from the constriction of flow passage and the hydrodynamic developing region; The f_xRe presents a back-and-forth motion around a reference curve for MCHS-AFR due to the larger changed flow passage as shown in Fig. 4, and the vibration amplitude becomes a little smaller with the increase W_r/S_r as the changed pressure.

Figures 6a and 6b show the effect of H_r on p_x and f_xRe along the flow direction as Re = 443, respectively. The geometry parameter used in these figures are W_c = 0.1 mm, S_r = 0.4 mm, W_r = 0.1 mm, and H_r = 0.005, 0.015 and 0.025 mm. It is noted that the height of fan-shaped ribs has a significant influence on the local pressure characteristics. From Fig. 6a, it can be seen that the p_x at a given position largely increases with the increase of H_r/W_c. The MCHS-AFR shows much higher p_x than MCHS-OFR with increase of H_r/W_c, while almost

the same as H_r/W_c = 0.05. Further, as H_r/W_c = 0.05, there is no obvious pressure fluctuation with the changed flow passage, but with increase of H_r/W_c, the p_x shows larger fluctuation, indicating that only the H_r/W_c is large enough, does the obvious pressure fluctuation occur. Along the whole length of microchannel, the Δp is 50.33, 77.05 and 179.76 kPa respectively for MCHS-AFR with H_r/W_c = 0.05, 0.15 and 0.25, while 49.33, 67.38 and 109.97 kPa respectively for MCHS-OFR with H_r/W_c = 0.05, 0.15 and 0.25. Corresponding to the p_x variation along the flow direction, the following phenomena for f_xRe with x^+ could be identified. As H_r/W_c = 0.05, the f_xRe at a given position is almost the same for MCHS-AFR and MCHS-OFR and just a little higher than the MCHS; With increase of H_r/W_c, the f_xRe extremely increases for MCHS-AFR, larger than MCHS-OFR; The larger H_r/W_c leads to the higher f_xRe at the microchannel inlet, due to the increased constriction to expansion ration of flow passage.

Figures 7a and 7b show the effect of S_r on p_x and f_xRe along the flow direction as Re = 443, respectively. The geometry parameters used in these figures are W_c = 0.1 mm, W_r = 0.1 mm, H_r = 0.025 mm and S_r = 2, 1, 0.5, and 0.25 mm. From Fig. 7a, it can be seen that the spacing of fan-shaped ribs has an important influence on the local pressure characteristics. The p_x at a given position largely increases with the decrease of S_r/W_c for both MCHS-AFR and MCHS-OFR. The lower S_r/W_c results in the larger pressure fluctuation as water flows cross the fan-shaped ribs, especially for the MCHS-AFR. Along the whole length of microchannel, the Δp is 70.24, 97.31, 154.98 and 248.35 kPa respectively for MCHS-AFR with S_r/W_c = 20, 10, 5 and 2.5, while 56.05, 68.67, 101.79 and 174.75 kPa respectively for MCHS-OFR with S_r/W_c = 20, 10, 5 and 2.5. Correspondingly, as shown in Fig. 7b, the lower

S_r/W_c leads to the larger fluctuation of f_xRe, especially for the MCHS-AFR; For the cases with S_r/W_c = 20 and 10, the f_xRe with x^+ coincides with MCHS at the channel inlet due to the hydrodynamic developing region for both MCHS-AFR and MCHS-OFR; For the cases with S_r/W_c = 5 and 2.5, the f_xRe with x^+ at the channel inlet is different from those with S_r/W_c = 20 and 10 for both MCHS-AFR and MCHS-OFR, due to the short smooth cross section region, where the effect of fan-shaped ribs on pressure characteristic has started.

3.2. Parametric study on average hydraulic characteristics

Figure 8 shows the effect of Re and W_r/S_r on $\overline{f}Re$ and $\overline{f}/\overline{f}_0$, where $\overline{f}_0$ is the average Fanning friction factor for the baseline MCHS. The geometry of fan-shaped ribs used in these figures is W_c = 0.1 mm, H_r = 0.025 mm, S_r = 0.4 mm and W_r = 0.05-0.4 mm. It can be seen that the fan-shaped ribs result in large pressure drop, especially for the MCHS-AFR. From Fig. 8a, it is noted that the $\overline{f}Re$ obviously increases with increase of Re. For the cases with W_r/S_r = 0.25, the increase rate of $\overline{f}Re$ with Re is evidently larger than the ones with W_r/S_r = 0.5, 0.75 and 1, for both MCHS-AFR and MCHS-OFR. Further, the increase rate of $\overline{f}Re$ with Re becomes lower with increase of W_r/S_r for MCHS-AFR, while almost the same for MCHS-OFR, as W_r/S_r = 0.5, 0.75 and 1. With the increase of Re from 187 to 715, the $\overline{f}Re$ increases from 13.27 to 16.04 for MCHS; from 39.4 to 81.26, 50.17 to 79.92, 60.45 to 85.23 and 70.65 to 88.35 respectively for MCHS-AFR with W_r/S_r = 0.25, 0.5, 0.75 and 1; from 27.82 to 47.43, 32.07 to 47.34, 43.63 to 61.24 and 58.54 to 74.29 respectively for MCHS-OFR with W_r/S_r = 0.25, 0.5, 0.75 and 1. As shown in Fig. 8b, the W_r/S_r has large influence on $\overline{f}/\overline{f}_0$ for the studied geometry parameters. Generally, the $\overline{f}/\overline{f}_0$ first decreases

and then increases with the increase of W_r/S_r, the turning point is in the range of from 0.1875 to 0.4375, which appears earlier for larger *Re*. The $\overline{f}/\overline{f}_0$ shows larger difference with *Re* for lower W_r/S_r, and the difference becomes smaller with increase of W_r/S_r. The MCHS-AFR shows larger $\overline{f}/\overline{f}_0$ difference with *Re* than MCHS-OFR. With the increase of W_r/S_r from 0.125 to 1, the $\overline{f}/\overline{f}_0$ of MCHS-AFR changes from 3.23 to 3.01 then 5.32, 4.04 to 3.35 then 5.38, 4.94 to 3.87 then 5.46, 5.79 to 4.37 then 5.48 and 6.62 to 4.86 then 5.51 respectively for *Re* = 187, 316, 443, 582 and 715, while the $\overline{f}/\overline{f}_0$ of MCHS-OFR changes from 2.17 to 2.07 then 4.41, 2.55 to 2.24 then 4.42, 2.97 to 2.46 then 4.53, 3.34 to 2.67 then 4.59 and 3.67 to 2.82 then 4.63 respectively for *Re* = 187, 316, 443, 582 and 715.

Figure 9 shows the effect of *Re* and H_r/W_c on $\overline{f}Re$ and $\overline{f}/\overline{f}_0$. The geometry of fan-shaped ribs used in these figures is W_c = 0.1 mm, S_r = 0.4 mm, W_r = 0.1 mm and H_r = 0.005-0.025 mm. As shown in Fig. 9a, the increase of H_r/W_c results in large increase of $\overline{f}Re$, especially for the MCHS-AFR. With the increase of *Re* from 187 to 715, the $\overline{f}Re$ increases from 15.25 to 18.2, 20.92 to 34.49 and 39.99 to 81.26 respectively for MCHS-AFR with H_r/W_c = 0.05, 0.15 and 0.25; from 15.07 to 17.75, 18.78 to 26.43 and 27.82 to 47.43 respectively for MCHS-OFR with H_r/W_c = 0.05, 0.15 and 0.25. From Fig. 9b, it is noticed that as H_r/W_c = 0.05, the $\overline{f}/\overline{f}_0$ is almost the same not only for both MCHS-AFR and MCHS-OFR but also for the studied Reynolds number; The increase of H_r/W_c leads to increase of $\overline{f}/\overline{f}_0$; The increase rate of $\overline{f}/\overline{f}_0$ becomes larger with increase of H_r/W_c; The larger H_r/W_c results in much higher $\overline{f}/\overline{f}_0$ for MCHS-AFR than MCHS-OFR. With the increase of H_r/W_c from 0.05 to 0.25, the $\overline{f}/\overline{f}_0$ increases from 1.15 to 3.01, 1.12 to 3.43, 1.12 to 4.01, 1.13 to 4.45 and 1.13 to 5.07 for MCHS-AFR respectively at *Re* = 187, 316, 443, 582 and 715; from 1.13 to 2.09, 1.1 to

2.46, 1.1 to 2.71, 1.11 to 2.96 for MCHS-OFR respectively at Re = 187, 316, 443, 582 and 715.

Figure 10 shows the effect of Re and S_r/W_c on $\overline{f}Re$ and $\overline{f}/\overline{f}_0$. The geometry of fan-shaped ribs used in these figures is W_c = 0.1 mm, W_r = 0.1 mm, H_r = 0.025 mm and S_r = 0.2-5 mm. It can be seen that the decrease of S_r/W_c results in large increase of $\overline{f}Re$, and the MCHS-AFR shows obviously larger $\overline{f}Re$ than MCHS-OFR, and the increase rate of $\overline{f}Re$ with Re is larger for MCHS-AFR than MCHS-OFR. Further, the decrease of S_r/W_c results in larger increase rate of $\overline{f}Re$ with Re. With the increase of Re from 187 to 715, the $\overline{f}Re$ increases from 19.1 to 29.16, 24.41 to 43.83, 34.75 to 70.31 and 53.92 to 125.44 respectively for MCHS-AFR with S_r/W_c = 20, 10, 5 and 2.5; from 16.25 to 21, 18.93 to 27.33, 25.54 to 39.09 and 40.24 to 72.59 respectively for MCHS-AFR with S_r/W_c = 20, 10, 5 and 2.5. As shown in Fig. 10b, the $\overline{f}/\overline{f}_0$ generally increases with the decrease of S_r/W_c. The decrease of S_r/W_c means the increase of number of fan-shaped ribs, and the fan-shaped ribs can keep the shorter smooth cross section region at higher hhydrodynamic developing level and thus the larger pressure drop penalty. With the decrease of S_r/W_c from 50 to 2, the $\overline{f}/\overline{f}_0$ increases from 1.2 to 4.88, 1.19 to 5.63, 1.22 to 6.48, 1.26 to 7.12 and 1.31 to 8.28 for MCHS-AFR respectively for Re = 187, 316, 443, 582 and 715; from 1.23 to 3.91, 1.22 to 4.53, 1.26 to 5.16, 1.3 to 5.68 and 1.34 to 6.27 for MCHS-OFR respectively for Re = 187, 316, 443, 582 and 715.

Based on the numerical results, the correlations of pressure drop for the microchannel heat sinks with different fan-shaped ribs on sidewalls are deduced by least squares method and shown as follows:

MCHS-AFR: $$\overline{f}Re = 103.8139 Re^{0.2902} (W_r/S_r)^{0.15} (H_r/W_c)^{0.9338} (S_r/W_c)^{-0.5731} \quad (12)$$

MCHS-OFR: $\overline{f}Re = 28.1081Re^{0.2956}(W_r/S_r)^{0.2657}(H_r/W_c)^{0.6412}(S_r/W_c)^{-0.1505}$ (13)

for $187 \le Re \le 715$, $0.02 \le W_r/S_r \le 1$, $0.05 \le H_r/W_c \le 0.25$, $2 \le S_r/W_c \le 50$

Figure 11 compares predictions of these correlations with the present CFD (Computational Fluid Dynamics) simulated data. The predictive accuracy of the correlations is measured by mean absolute error, which is defined as

$$\mathrm{MAE} = \frac{1}{N}\sum_{i=1}^{N}\frac{\left|\overline{Nu}_{\mathrm{pred}} - \overline{Nu}_{\mathrm{cfd}}\right|}{\overline{Nu}_{\mathrm{cfd}}} \times 100\% \quad (14)$$

It can be found that most data points are shown falling within ±20% error bands, with MAE = 13.2% for MCHS-AFR and MAE = 13.5% for MCHS-OFR.

4. Conclusions

Laminar flow hydraulic characteristics in microchannel heat sinks with fan-shaped ribs in tandem, aligned and offset arrangements on two opposite sidewalls have been investigated numerically. The effect of fan-shaped ribs' geometry on local and average hydraulic characteristics has been investigated. According to the numerical results, concluding remarks are drawn as follow:

(1). The local laminar flow hydraulic characteristics are mainly dependent on the changed flow passage for MCHS-AFR, while both the changed flow passage and the periodically changed flow direction for MCHS-OFR. For the local pressure and friction factor of MCHS-AFR, the increase of W_r/S_r leads to smaller fluctuation amplitude, the increase of H_r/W_c results in obviously larger fluctuation amplitude, and the decrease of S_r/W_c causes decrease of fluctuation amplitude.

(2). The geometric parameters of fan-shaped ribs have significant influence on average

hydraulic characteristics of laminar flow in such microchannels. With the increase of W_r/S_r, the $\overline{f}/\overline{f}_0$ first decreases and then increases, and the turning points are in the range of from 0.1875 to 0.4375. The increase of H_r/W_c and decrease of S_r/W_c lead to obvious increase of $\overline{f}/\overline{f}_0$. With increase of H_r/W_c and decrease of S_r/W_c, the MCHS-AFR shows much higher $\overline{f}/\overline{f}_0$ than MCHS-OFR.

(3). For Reynolds number ranging from 187 to 715, as W_c = 0.1 mm, H_r = 0.025 mm and S_r = 0.4 mm, with the increase of W_r/S_r from 0.125 to 1, the $\overline{f}/\overline{f}_0$ changes in the ranges of 3.01-5.51 for MCHS-AFR and 2.07-4.63 for MCHS-OFR; As W_c = 0.1 mm, S_r = 0.4 mm and W_r = 0.1 mm, with the increase of H_r/W_c from 0.05 to 0.25, the $\overline{f}/\overline{f}_0$ changes from 1.12 to 5.07 for MCHS-AFR and 1.1 to 2.96 for MCHS-OFR; As W_c = 0.1 mm, W_r = 0.1 mm and H_r = 0.025 mm, with the decrease of S_r/W_c from 50 to 2, the $\overline{f}/\overline{f}_0$ changes from 1.19 to 8.28 for MCHS-AFR and 1.22 to 6.27 for MCHS-OFR.

(4). New pressure drop correlations for the microchannel heat sinks with different fan-shaped ribs on sidewalls are proposed, which fit the present CFD simulated data with a mean absolute error of 13.2% for MCHS-AFR and 13.5% for MCHS-OFR..

Acknowledgements

The work was supported by the Engineering and Physical Sciences Research Council (EPSRC) of the UK through research grant (EP/L001233/1) and the National Natural Science Foundation of China (51576005).

References

[1] S. Kandlikar, S. Garimella, D. Li, S. Colin, M.R. King, Heat transfer and fluid flow in minichannels and microchannels. Elsevier, 2005.

[2] G.M. Mala, D. Li, Flow characteristics of water in microtubes, International Journal of Heat and Fluid Flow 20 (1999) 142-148.

[3] M.E. Steinke, S.G. Kandlikar, Single–phase liquid friction factors in microchannels, International Journal of Thermal Sciences 45 (2006) 1073–1083.

[4] J.L. Xu, Y.H. Gan, D.C. Zhang, Microscale heat transfer enhancement using thermal boundary layer redeveloping concept, International Journal of Heat and Mass Transfer 48 (2005) 1662–1674.

[5] J.L. Xu, Y.X. Song, W Zhang, Numerical simulations of interrupted and conventional microchannel heat sinks, International Journal of Heat and Mass Transfer 51 (2008) 5906–5917.

[6] L. Chai, G.D. Xia, M.Z. Zhou, Optimum thermal design of interrupted microchannel heat sink with rectangular ribs in the transverse microchambers, Applied Thermal Engineering 51 (2013) 880–989.

[7] P. Promvonge, S. Sripattanapipat, S. Kwankaomeng, Laminar periodic flow and heat transfer in square channel with 45º inline baffles on two opposite walls, International Journal of Thermal Sciences 49 (2010) 963–975.

[8] C. Liu, J. Teng, J.C. Chu, Experimental investigations on liquid flow and heat transfer

in rectangular microchannel with longitudinal vortex generators, International Journal of Heat and Mass Transfer 54 (2011) 3069–3080.

[9] A. Ebrahimi, R. Ehsan Roohi, K. Saeid, Numerical study of liquid flow and heat transfer in rectangular microchannel with longitudinal vortex generators, Applied Thermal Engineering 78 (2015) 576–583.

[10] L. Chai, G.D. Xia, M.Z. Zhou, Numerical simulation of fluid flow and heat transfer in a microchannel heat sink with offset fan-shaped reentrant cavities in sidewall, International Communications in Heat and Mass Transfer 38 (2011) 577–584.

[11] L. Chai, G.D. Xia, L. Wang, M.Z. Zhou, Z.Z. Cui, Heat transfer enhancement in microchannel heat sinks with periodic expansion–constriction cross-sections, International Journal of Heat and Mass Transfer 62 (2013) 741–751.

[12] G.D. Xia, L. Chai, M.Z. Zhou, Effects of structural parameters on fluid flow and heat transfer in a microchannel with aligned fan-shaped reentrant cavities, International Journal of Thermal Sciences 50 (2011) 411–419.

[13] G.D. Xia, L. Chai, H.Y. Wang, Optimum thermal design of microchannel heat sink with triangular reentrant cavities, Applied Thermal Engineering 31 (2011) 1208–1219.

[14] H. Ghaedamini, P.S. Lee, C.J. Teo, Developing forced convection in converging–diverging microchannels, International Journal of Heat and Mass Transfer 65 (2013) 491–499.

[15] Y. Sui, C.J. Teo, P.S. Lee, Fluid flow and heat transfer in wavy microchannels, International Journal of Heat and Mass Transfer 53 (2010) 2760–2772.

[16] Y. Sui, P.S. Lee, C.J. Teo, An experimental study of flow friction and heat transfer in

wavy microchannels with rectangular cross section, International Journal of Thermal Sciences 50 (2011) 2473–2482.

[17] H.A. Mohammed, P. Gunnasegaran, N.H. Shuaib, Numerical simulation of heat transfer enhancement in wavy microchannel heat sink, International Communications in Heat and Mass Transfer 38 (2011) 63–68.

[18] L. Chai, G.D. Xia, H.S. Wang, Numerical study of laminar flow and heat transfer in microchannel heat sink with offset ribs on sidewalls, Applied Thermal Engineering 92 (2016) 32–41.

[19] F. Incropera, Liquid Cooling of Electronic Devices by Single-Phase Convection, Wiley, 1999.

[20] R.J. Phillips, Forced convection, liquid cooled, microchannel heat sinks, MS Thesis, Department of Mechanical Engineering, Massachusetts Institute of Technology, Cambridge, MA, 1987.

Nomenclature

c_p	Specific heat capacity, $J \cdot kg^{-1} K^{-1}$
D_h	Hydraulic diameter, m
f	Friction factor
$\overline{f}$	Average friction factor
$\overline{f}_0$	Average friction factor for the smooth microchannel
H	Height, m
k	Thermal conductivity, $W \cdot m^{-1} \cdot K^{-1}$
L	Length, m
MAE	mean absolute error
p	Pressure, Pa
Δp	Pressure drop, Pa
q_w	Heat flux, $W \cdot m^{-2}$
Re	Reynolds number
$\vec{u}$	Fluid velocity vector
$\overline{u}$	Average velocity, $m \cdot s^{-1}$
V	Volume, m^3
W	Width, m
x, y, z	Cartesian coordinates, m
Greek letters	
ρ	Density, $kg \cdot m^{-3}$

μ	Dynamic viscosity, Pa·s
Subscripts	
c	Channel
f	Fluid
in	Inlet
out	Outlet
r	Rib
s	Solid

Figure captions

Fig. 1 Geometry and definitions of microchannel heat sinks with fan-shaped ribs on sidewalls. (a) Computational domain. (b) Geometric parameters of fan-shaped ribs.

Fig. 2 Verification of mathematical model for average friction factor in smooth microchannel heat sink.

Fig. 3 Pressure distribution (Re = 443, z = 0.25 mm, W_c = 0.1 mm, W_r = 0.1 mm, H_r = 0.025 mm and S_r = 0.4 mm)

Fig. 4 Local pressure (Re = 443, z = 0.25 mm, W_c = 0.1 mm, W_r = 0.1 mm, H_r = 0.025 mm and S_r = 0.4 mm)

Fig. 5 Effects of fan-shaped rib's width on local hydraulic characteristics (Re = 443, W_c = 0.1 mm, H_r = 0.025 mm and S_r = 0.4 mm). (a) p_x versus x. (b) f_xRe versus x^+.

Fig. 6 Effects of fan-shaped rib's height on local hydraulic characteristics (Re = 443, W_c = 0.1 mm, S_r = 0.4 mm and W_r = 0.1 mm). (a) p_x versus x. (b) f_xRe versus x^+.

Fig. 7 Effects of fan-shaped rib's spacing on local hydraulic characteristics (Re = 443, W_c = 0.1 mm, W_r = 0.1 mm and H_r = 0.025 mm). (a) p_x versus x. (b) f_xRe versus x^+.

Fig. 8 Effects of fan-shaped rib's width on average friction factor (W_c = 0.1 mm, H_r = 0.025 mm and S_r = 0.4 mm). (a) $\overline{f}Re$ versus Re. (b) $\overline{f}/\overline{f}_0$ versus W_r/S_r.

Fig. 9 Effects of fan-shaped rib's height on average friction factor (W_c = 0.1 mm, S_r = 0.4 mm and W_r = 0.1 mm). (a) $\overline{f}Re$ versus Re. (b) $\overline{f}/\overline{f}_0$ versus H_r/W_c.

Fig. 10 Effects of fan-shaped rib's spacing on average friction factor (W_c = 0.1 mm, W_r = 0.1 mm and H_r = 0.025 mm). (a) $\overline{f}Re$ versus Re. (b) $\overline{f}/\overline{f}_0$ versus S_r/W_c.

Fig. 11 Comparison of predictions of pressure drop correlations with the present CFD

simulated data. (a) MCHS-AFR. (b) MCHS-OFR.

Fig. 1

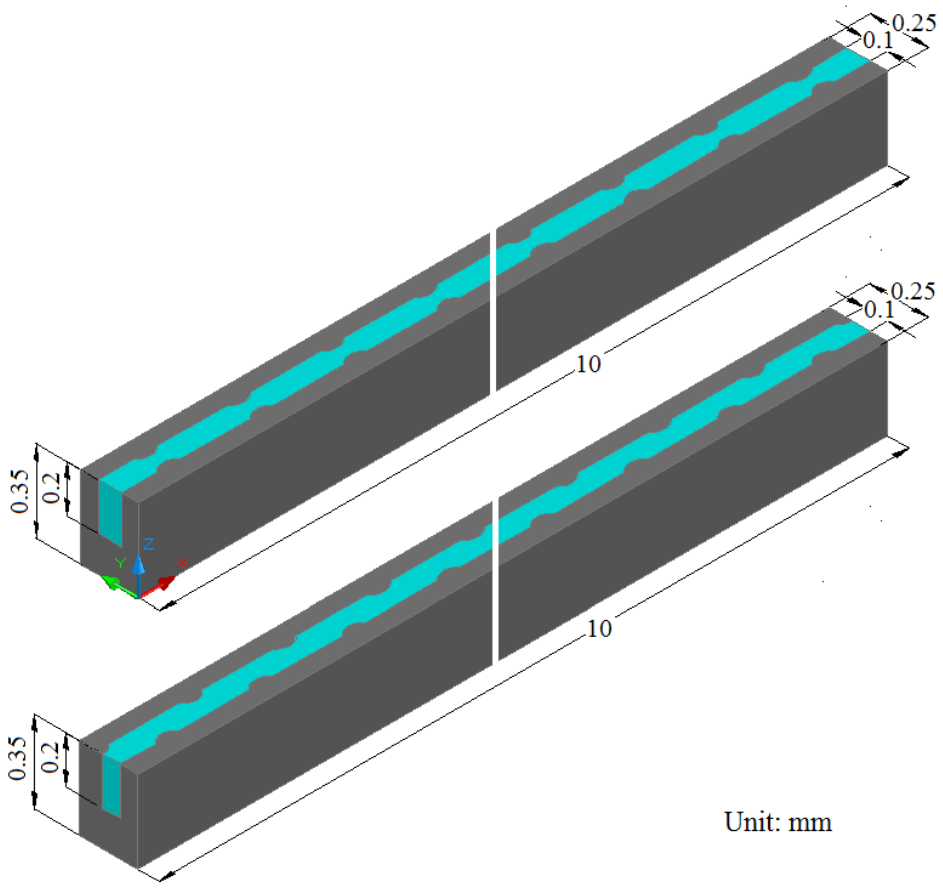
0.25
0.1
10
0.35
0.2
0.25
0.1
10
0.35
0.2
Unit: mm

(a)

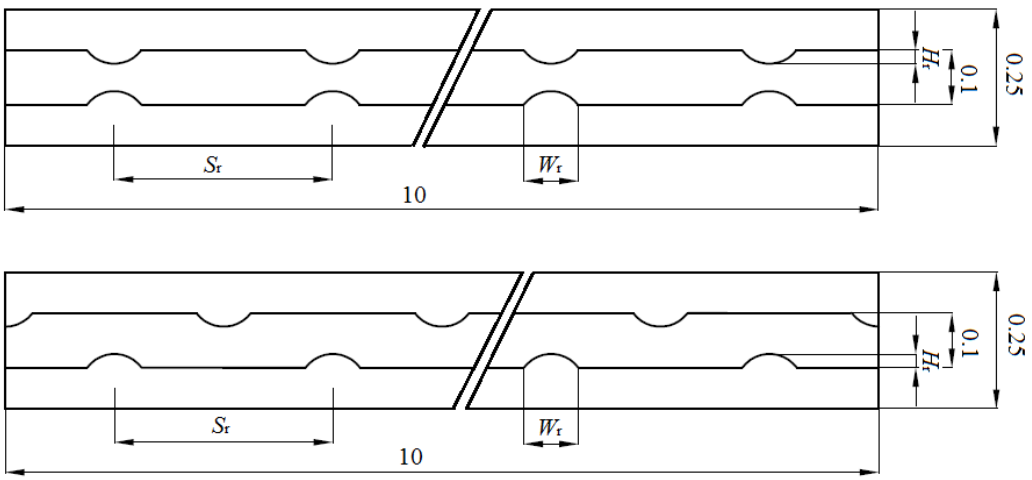
H_r
0.1
0.25
S_r
W_r
10
H_r
0.1
0.25
S_r
W_r
10
Unit: mm

(b)

Fig. 2

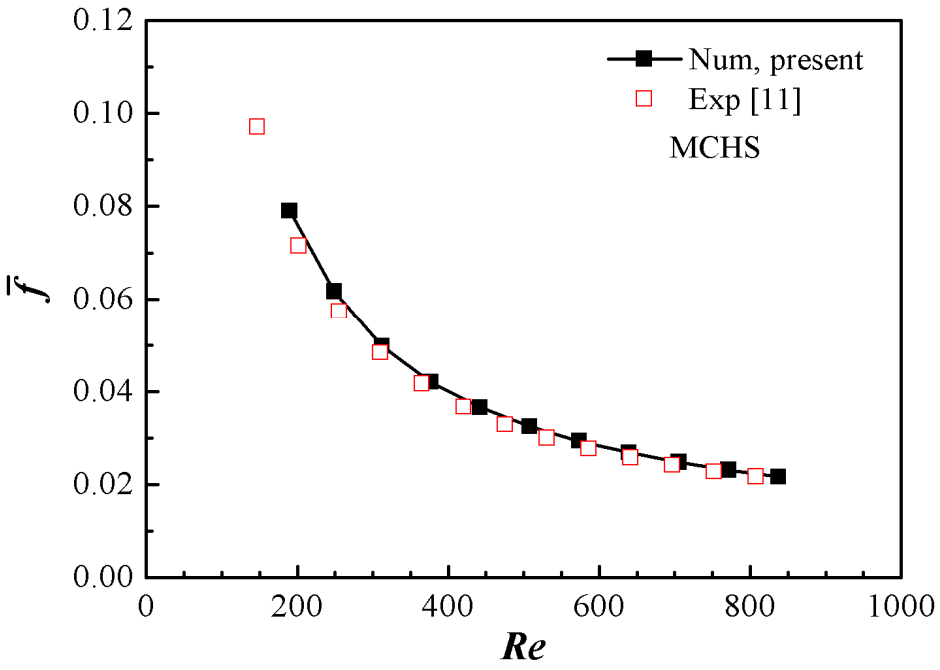
0.12
0.10
0.08
0.06
0.04
0.02
0.00
f
0
200
400
600
800
1000
Re
Num, present
Exp [11]
MCHS

Fig. 3

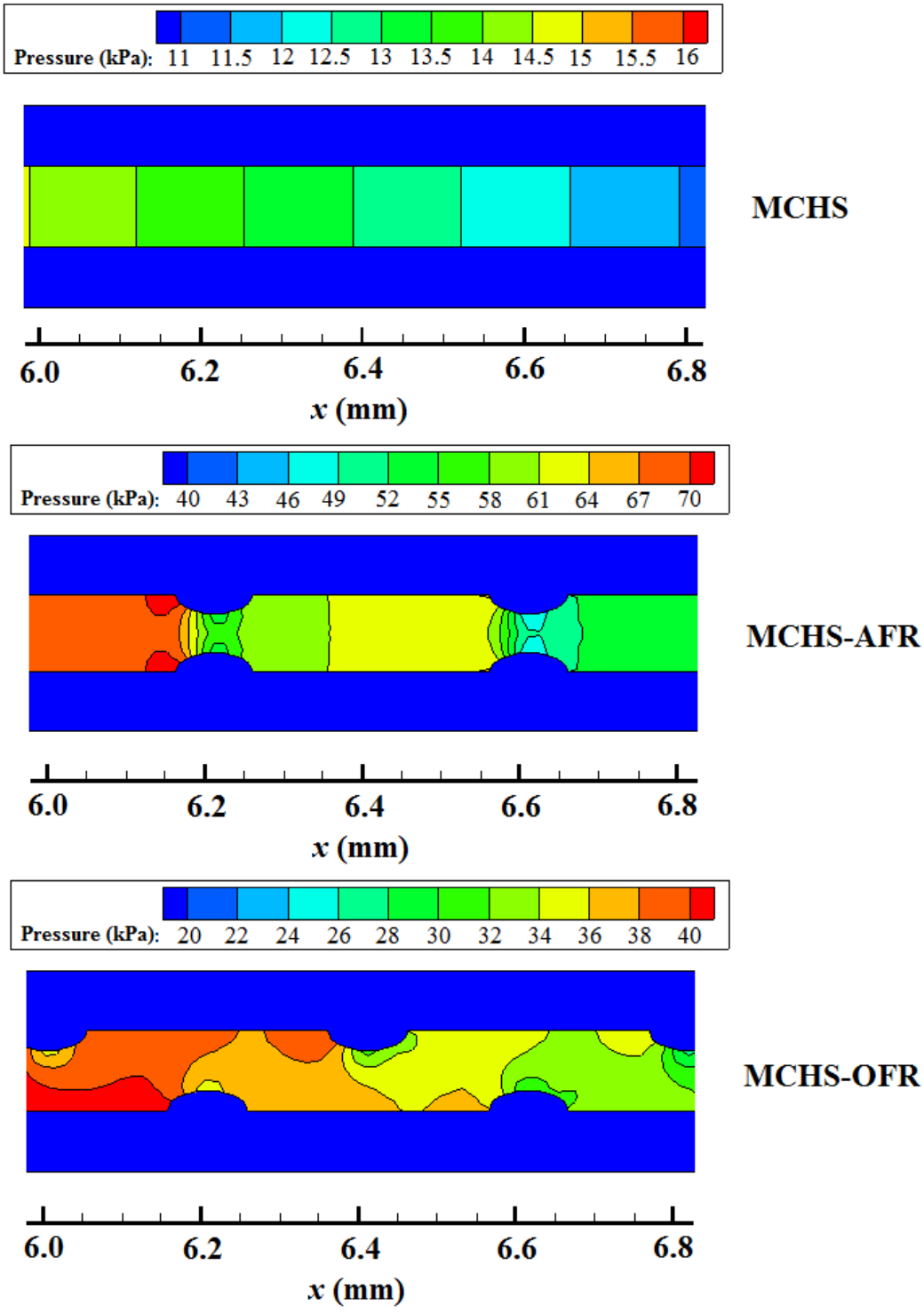
Pressure (kPa): 11 11.5 12 12.5 13 13.5 14 14.5 15 15.5 16
MCHS
6.0 6.2 6.4 6.6 6.8
x (mm)
Pressure (kPa): 40 43 46 49 52 55 58 61 64 67 70
MCHS-AFR
6.0 6.2 6.4 6.6 6.8
x (mm)
Pressure (kPa): 20 22 24 26 28 30 32 34 36 38 40
MCHS-OFR
6.0 6.2 6.4 6.6 6.8
x (mm)

Fig. 4

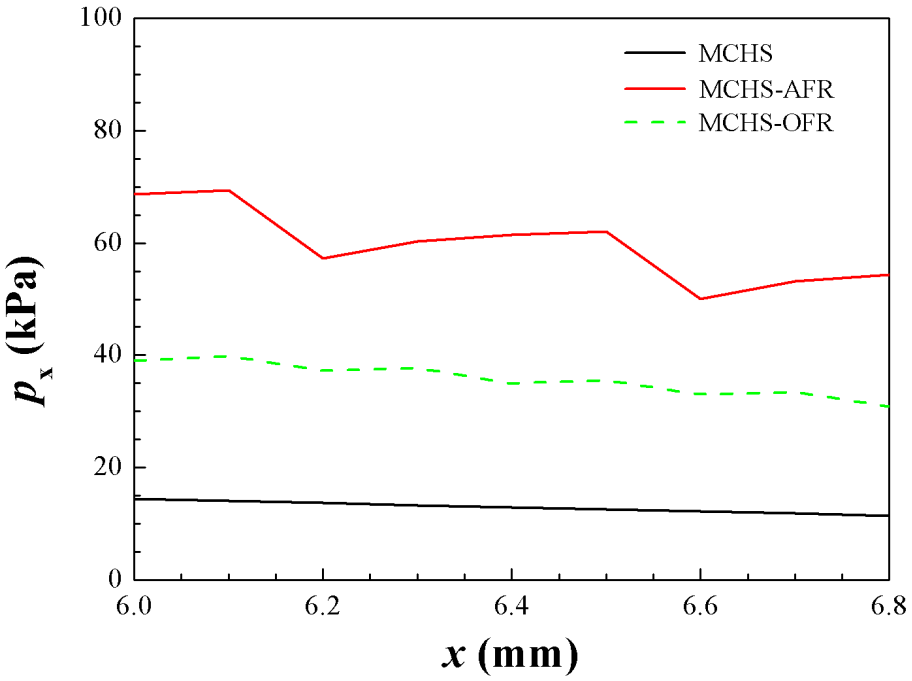

Fig. 5

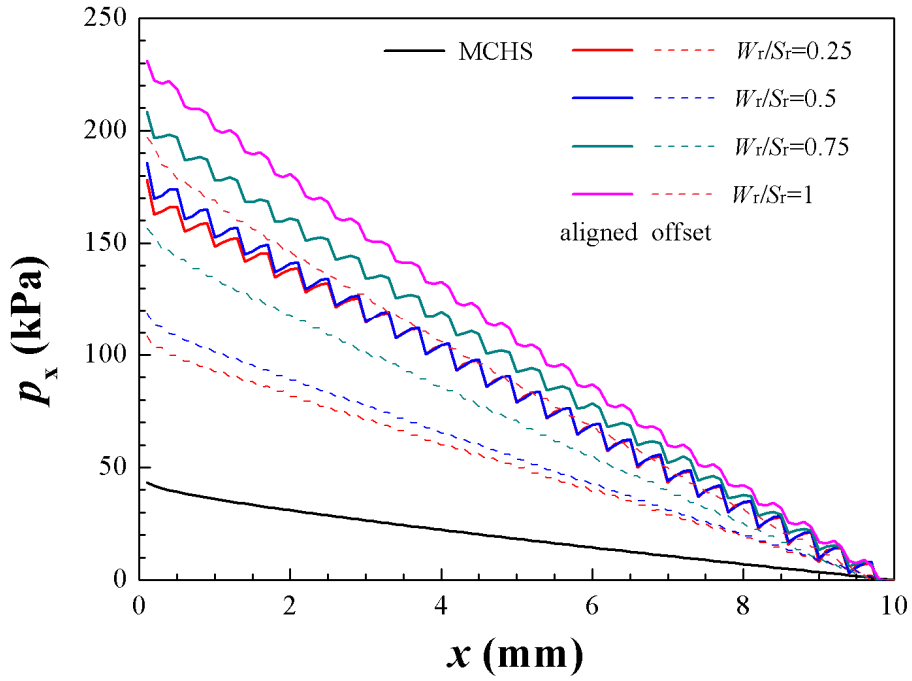
MCHS
W_r/S_r=0.25
W_r/S_r=0.5
W_r/S_r=0.75
W_r/S_r=1
aligned offset
p_x (kPa)
x (mm)
0
50
100
150
200
250
0
2
4
6
8
10

(a)

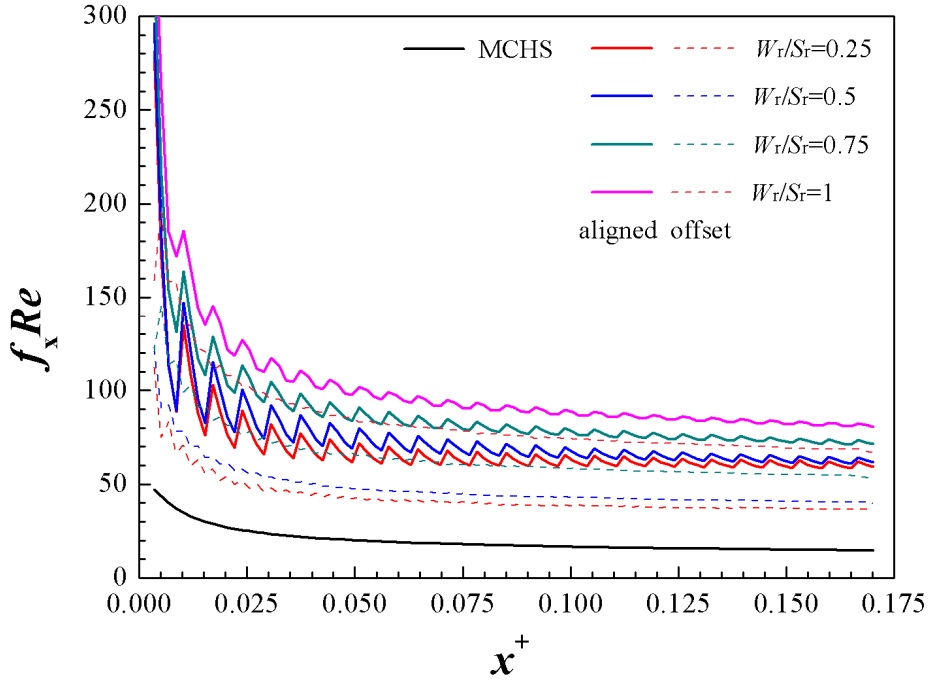
MCHS
W_r/S_r=0.25
W_r/S_r=0.5
W_r/S_r=0.75
W_r/S_r=1
aligned offset
$f_x Re$
x^+
0
50
100
150
200
250
300
0.000
0.025
0.050
0.075
0.100
0.125
0.150
0.175

(b)

Fig. 6

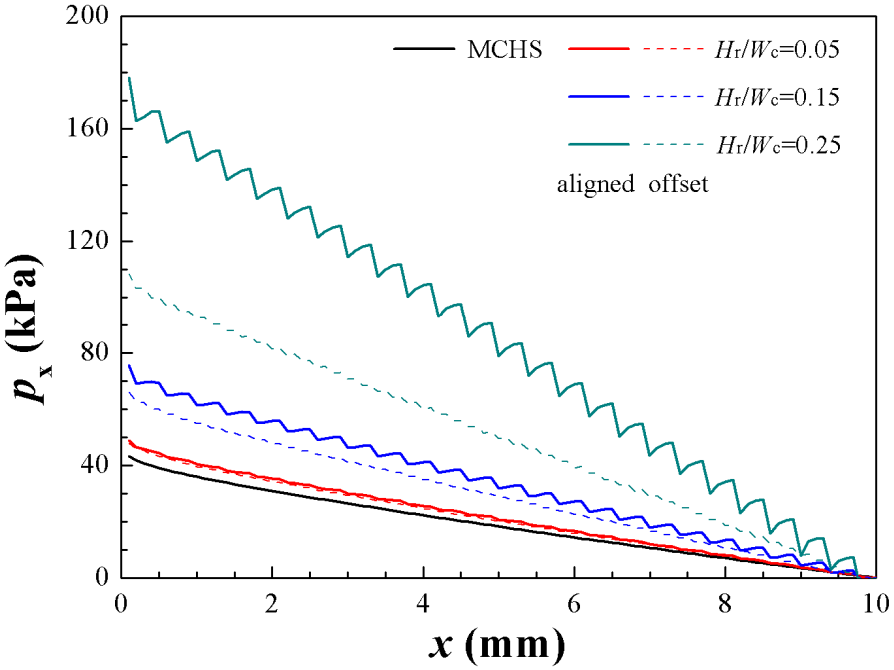
MCHS
H_r/W_c=0.05
H_r/W_c=0.15
H_r/W_c=0.25
aligned offset
p_x (kPa)
x (mm)
0
40
80
120
160
200
0
2
4
6
8
10

(a)

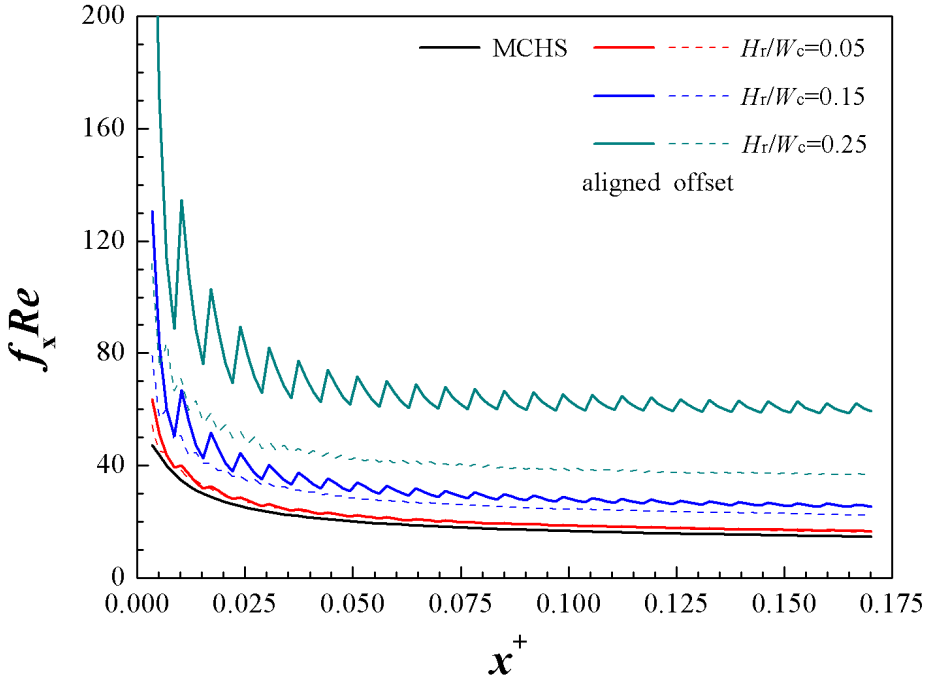
MCHS
H_r/W_c=0.05
H_r/W_c=0.15
H_r/W_c=0.25
aligned offset
$f_x Re$
x^+
0
40
80
120
160
200
0.000
0.025
0.050
0.075
0.100
0.125
0.150
0.175

(b)

Fig. 7

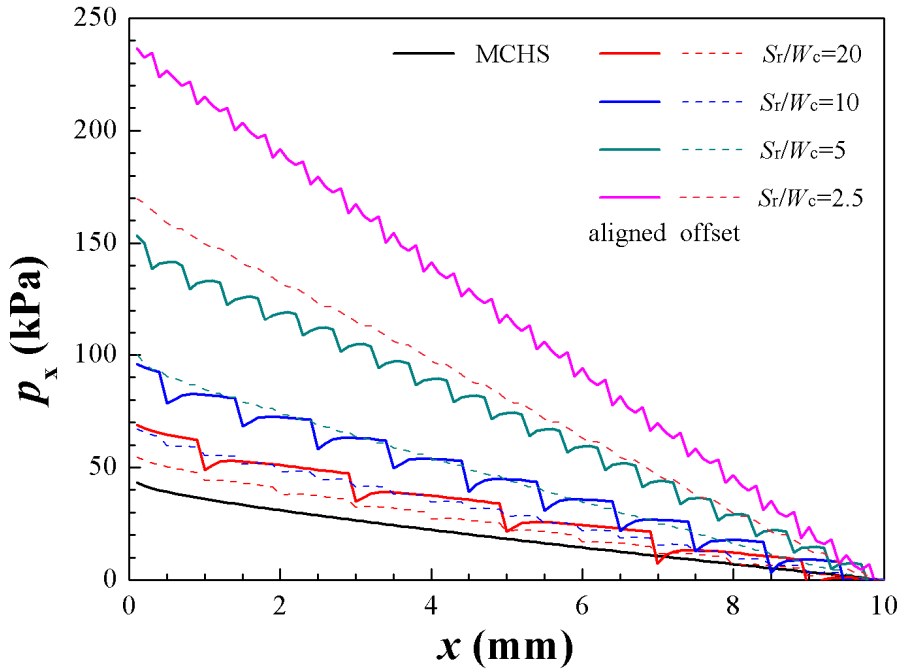
MCHS
Sr/Wc=20
Sr/Wc=10
Sr/Wc=5
Sr/Wc=2.5
aligned offset
p_x (kPa)
x (mm)
0
50
100
150
200
250
0
2
4
6
8
10

(a)

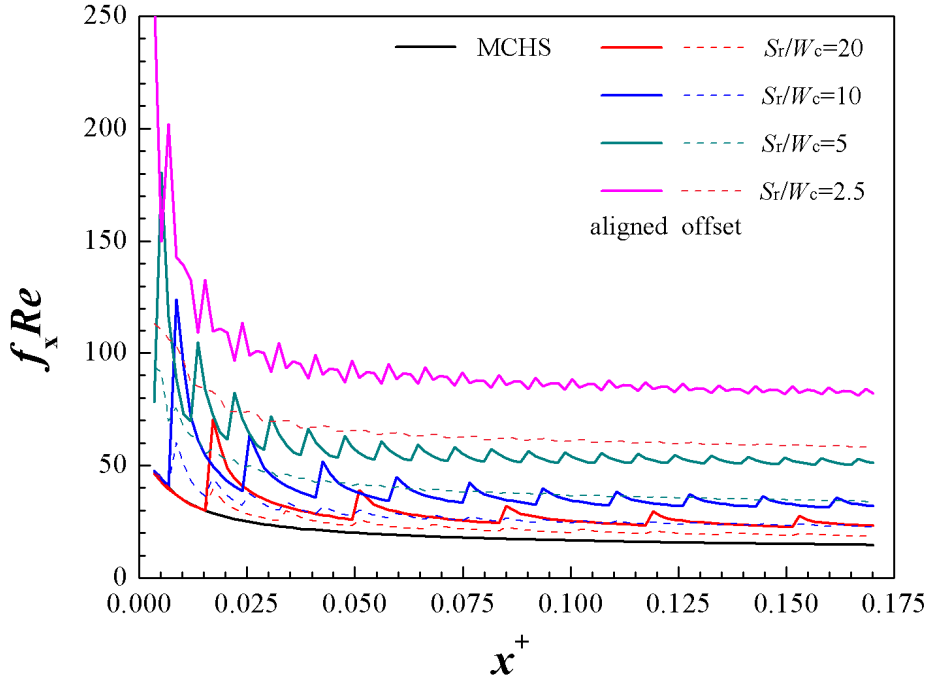
MCHS
Sr/Wc=20
Sr/Wc=10
Sr/Wc=5
Sr/Wc=2.5
aligned offset
f_x Re
x+
0
50
100
150
200
250
0.000
0.025
0.050
0.075
0.100
0.125
0.150
0.175

(b)

Fig. 8

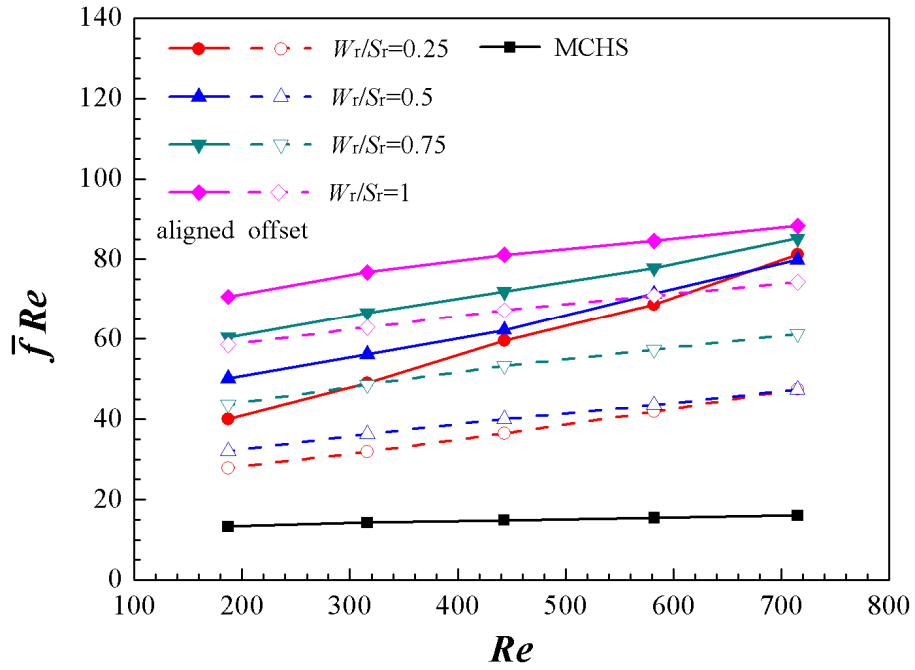
140
120
100
80
60
40
20
0
100
200
300
400
500
600
700
800
$\bar{f}Re$
Re
W_r/S_r=0.25
MCHS
W_r/S_r=0.5
W_r/S_r=0.75
W_r/S_r=1
aligned offset

(a)

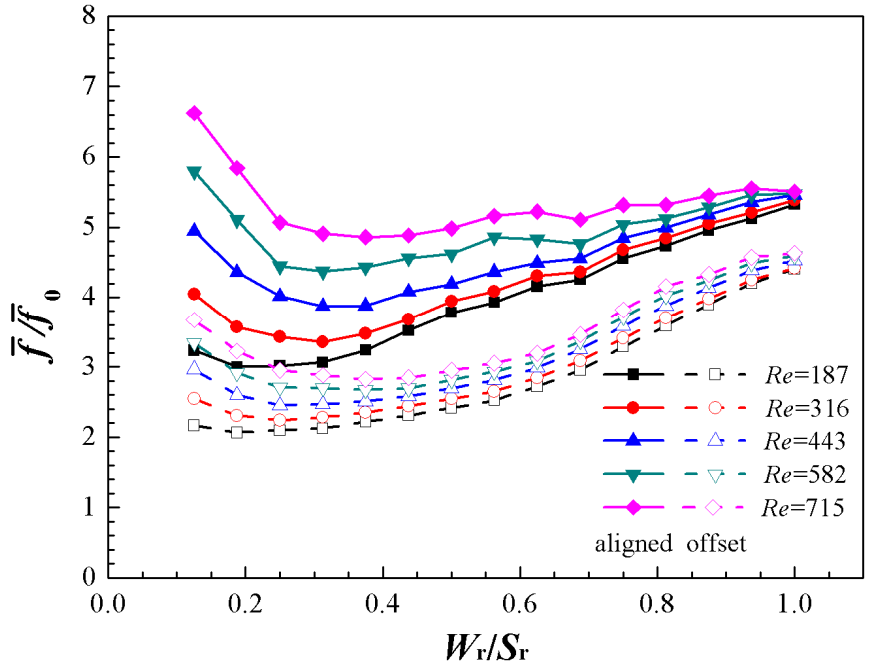
8
7
6
5
4
3
2
1
0
0.0
0.2
0.4
0.6
0.8
1.0
$\bar{f}/\bar{f}_0$
W_r/S_r
Re=187
Re=316
Re=443
Re=582
Re=715
aligned offset

(b)

Fig. 9

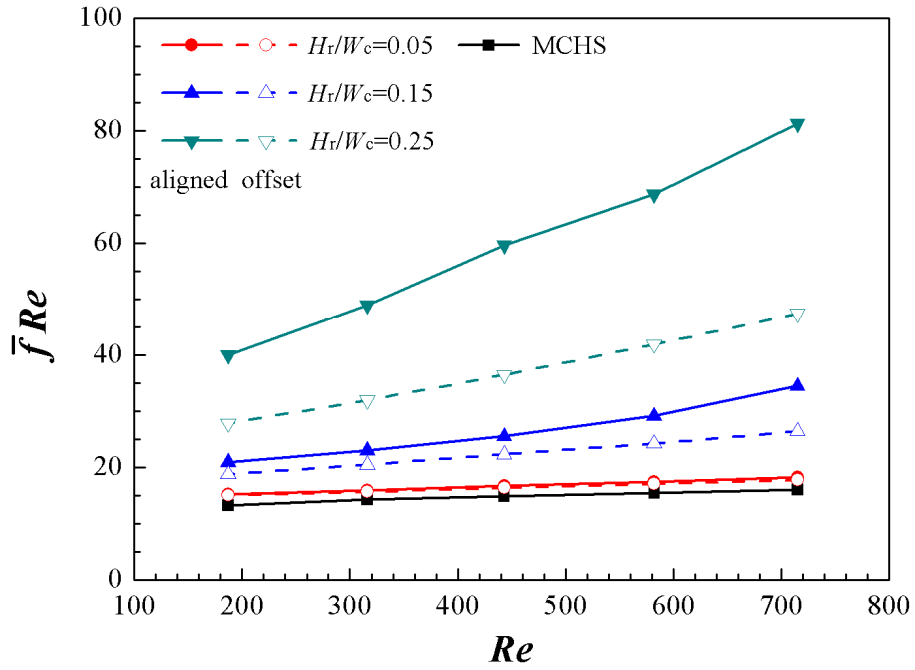
100
80
60
40
20
0
100
200
300
400
500
600
700
800
$\bar{f}Re$
Re
H_r/W_c=0.05
MCHS
H_r/W_c=0.15
H_r/W_c=0.25
aligned offset

(a)

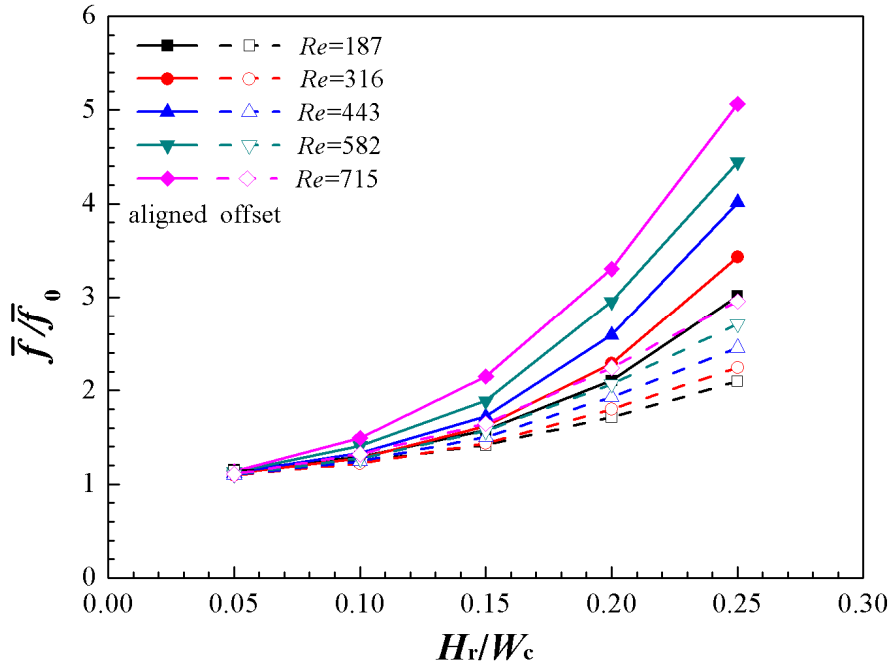
6
5
4
3
2
1
0
0.00
0.05
0.10
0.15
0.20
0.25
0.30
$\bar{f}/\bar{f}_0$
H_r/W_c
Re=187
Re=316
Re=443
Re=582
Re=715
aligned offset

(b)

Fig. 10

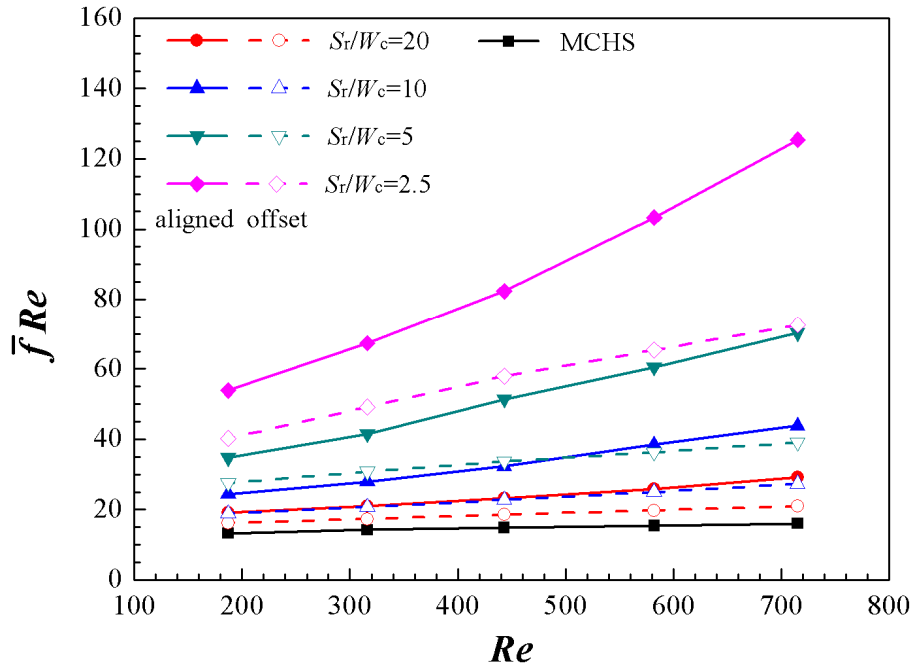
160
140
120
100
80
60
40
20
0
100
200
300
400
500
600
700
800
$\bar{f}Re$
Re
S_r/W_c=20
S_r/W_c=10
S_r/W_c=5
S_r/W_c=2.5
MCHS
aligned offset

(a)

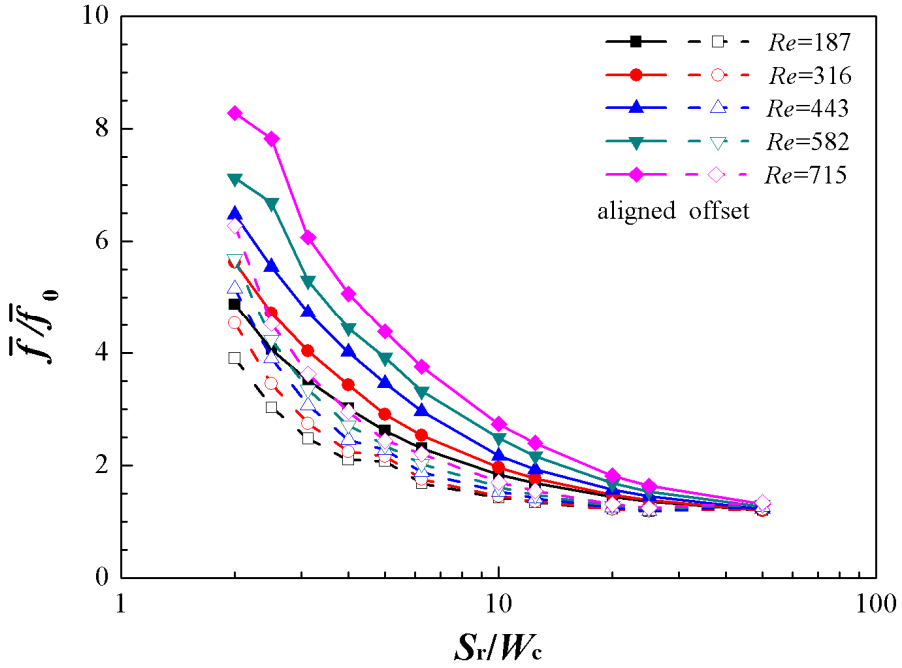
10
8
6
4
2
0
1
10
100
$\bar{f}/\bar{f}_0$
S_r/W_c
Re=187
Re=316
Re=443
Re=582
Re=715
aligned offset

(b)

Fig. 11

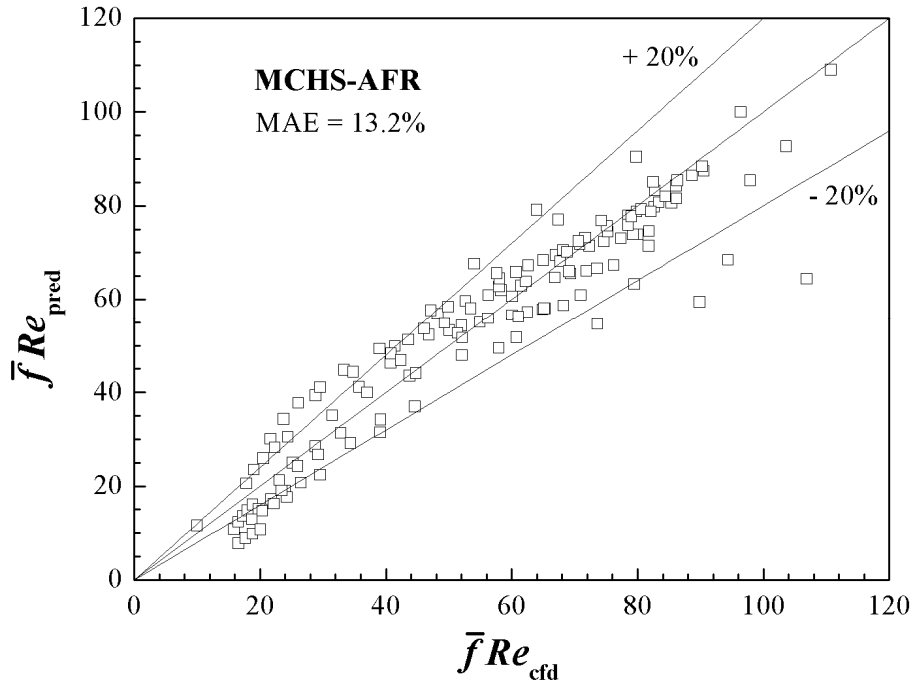
MCHS-AFR
MAE = 13.2%
+ 20%
- 20%
$\bar{f}Re_{pred}$
$\bar{f}Re_{cfd}$
0
20
40
60
80
100
120

(a)

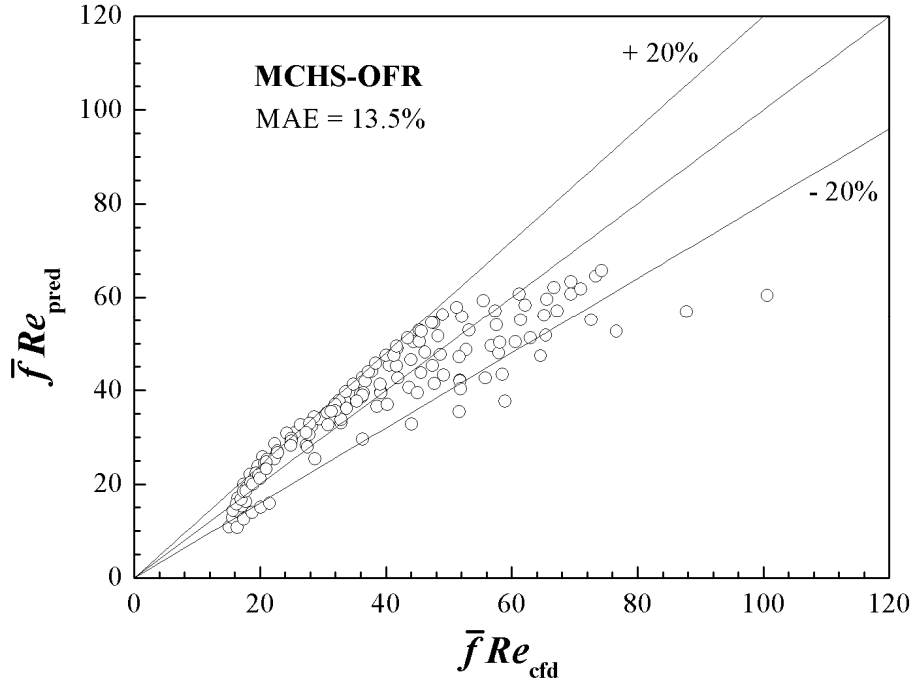
MCHS-OFR
MAE = 13.5%
+ 20%
- 20%
$\bar{f}Re_{pred}$
$\bar{f}Re_{cfd}$
0
20
40
60
80
100
120

(b)